Interaction between S4 and the phosphatase domain mediates electrochemical coupling in voltage-sensing phosphatase (VSP)

Natsuki Mizutani[a], Akira Kawanabe[a,1] (iD), Yuka Jinno[a,2], Hirotaka Narita[b,3], Tomoko Yonezawa[a,4], Atsushi Nakagawa[b] (iD), and Yasushi Okamura[a,c,5] (iD)

Voltage-sensing phosphatase (VSP) consists of a voltage sensor domain (VSD) and a cytoplasmic catalytic region (CCR), which is similar to phosphatase and tensin homolog (PTEN). How the VSD regulates the innate enzyme component of VSP remains unclear. Here, we took a combined approach that entailed the use of electrophysiology, fluorometry, and structural modeling to study the electrochemical coupling in *Ciona intestinalis* VSP. We found that two hydrophobic residues at the lowest part of S4 play an essential role in the later transition of VSD-CCR coupling. Voltage clamp fluorometry and disulfide bond locking indicated that S4 and its neighboring linker move as one helix (S4-linker helix) and approach the hydrophobic spine in the CCR, a structure located near the cell membrane and also conserved in PTEN. We propose that the hydrophobic spine operates as a hub for translating an electrical signal into a chemical one in VSP.

voltage-sensing phosphatase | voltage sensor domain | hydrophobicity | Anap | phosphoinositide

Conserved among the voltage-dependent membrane protein superfamily, the voltage sensor domain (VSD) is a specialized structure for detection of voltage changes across the plasma membrane. The VSD is composed of four helical transmembrane segments (S1 to S4), among which S4 has a unique structure consisting of positively charged amino acids periodically aligned at intervals with intervening pairs of hydrophobic amino acids. This structure enables S4 to exhibit marked voltage-dependent motility. Within voltage-gated ion channels (VGICs), the VSD regulates the downstream pore-gate domain (S5 and S6), which forms an ion permeation pathway. The VSD is tightly coupled to the pore-gate domain (1), and a linker between S4 and S5 (S4-S5 linker) regulates pore-gating (2–7).

Voltage-sensing phosphatase (VSP) also contains a VSD but lacks the transmembrane pore-gate domain. Instead, VSP contains the cytoplasmic catalytic region (CCR) with remarkable similarity to phosphatase and tensin homolog deleted on chromosome 10 (PTEN), which consists of a phosphatase domain (PD) and a C2 domain (8, 9) (Fig. 1*A*). VSP dephosphorylates mainly plasma membrane phosphatidylinositol 4,5-bisphosphate (PI(4,5)P$_2$) upon membrane depolarization (10, 11). In contrast to VGICs, which form a tetramer or possess a four-repeat structure within a single polypeptide, VSP can operate as a monomer. VSP genes are conserved in a wide variety of species, and VSP gene expression is found in the testis (9). Our recent study of mouse sperm revealed that VSP activity produces a polarized PI(4,5)P$_2$ distribution in the sperm flagellum to regulate maturation of sperm motility (12).

The VSD is tightly coupled to a downstream effector domain in VSP (10, 13–17), and several critical regions for coupling the VSD to the CCR have been identified (8, 15, 18–20). We have recently reported that the PD contains a hydrophobic structure called the hydrophobic spine (21), which is conserved in PTEN and VSP (Fig. 1*A*). Located near the interface of the plasma membrane and cytoplasm, substitution of a residue within the hydrophobic spine with a hydrophilic residue markedly diminishes coupling (21, 22). Voltage clamp fluorometry (VCF) of *Ciona intestinalis* VSP (Ci-VSP) with a fluorescent unnatural amino acid [3-(6-acetylnaphthalen-2-ylamino)-2-aminopropanoic acid (Anap)] incorporated at K555 within the CCR showed that the hydrophobic spine is essential for the later transition of the two steps of phosphatase activation (21). However, it remains unclear how the VSD and the hydrophobic spine interact to achieve coupling or how the operating mechanisms of VSP are related to those of PTEN.

In the present study, we analyzed in detail the motion of the lower part of S4 and the neighboring linker region by detecting local fluorescence after genetic incorporation of a fluorophore into Ci-VSP. We found that the two hydrophobic residues at the C-terminal end of S4, which are highly conserved among VSP orthologs, play a critical role in VSD-CCR coupling. We also found that upon membrane depolarization, a unit consisting of

---

[1]Present address: Laboratory of Molecular Physiology and Biophysics, Faculty of Medicine, Kagawa University, Miki-cho, Kagawa 761-0793, Japan.

[2]Present address: Department of Cardiovascular Medicine, Graduate School of Medicine, Osaka University, Suita, Osaka 565-0871, Japan.

[3]Present address: Japan Aerospace Exploration Agency, Tsukuba, Ibaraki 305-8505, Japan.

[4]Present address: Center for Medical Research and Education, Graduate School of Medicine, Osaka University, Suita, Osaka 565-0871, Japan.

[5]To whom correspondence may be addressed. Email: yokamura@phys2.med.osaka-u.ac.jp.
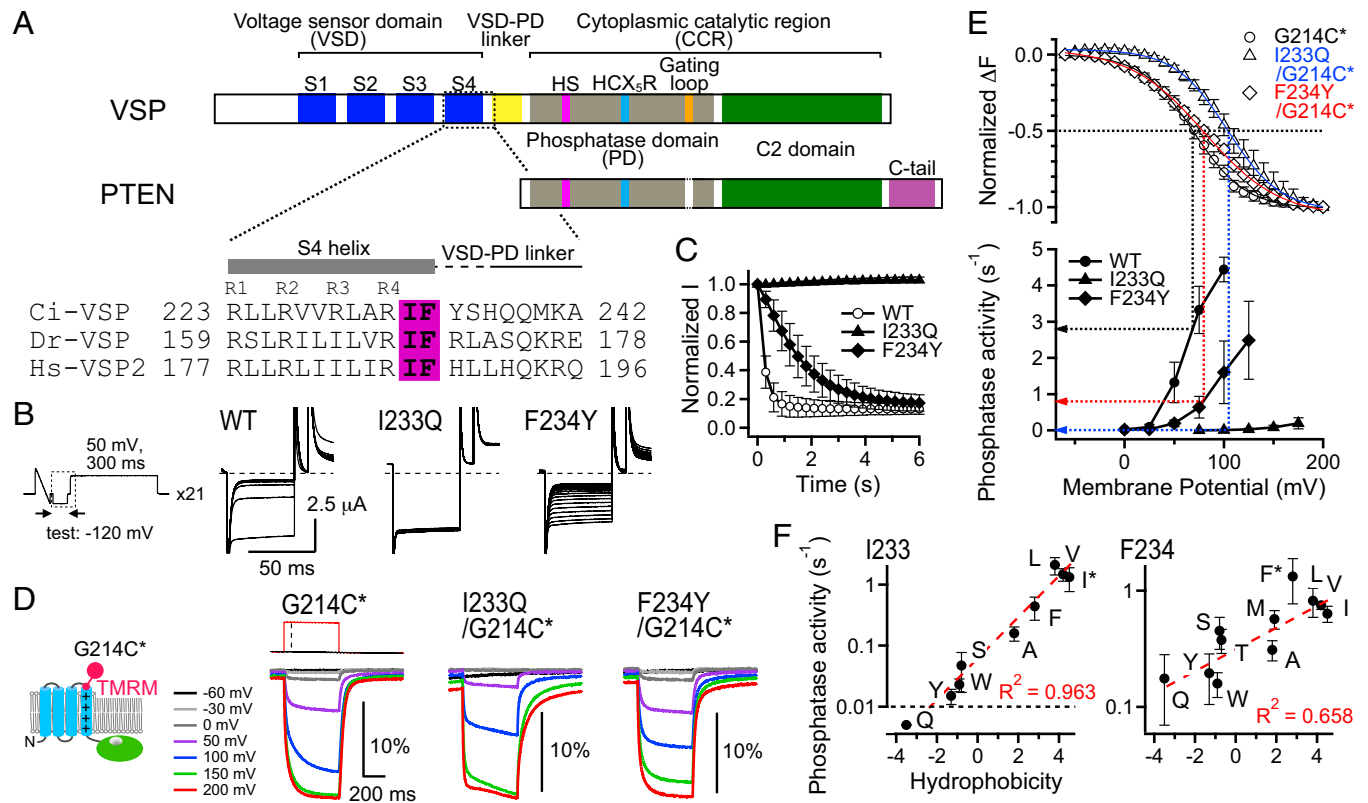
Fig. 1. Effect of the hydrophobicity at I233 and F234 within the C-terminal end of S4 on the phosphatase activity of Ci-VSP. (*A*) *Top*: Schematic of VSP and PTEN. Blue, VSD; yellow, VSD-PD linker; magenta, hydrophobic spine (HS); cyan, HCX$_5$R motif in the PD (gray); orange, gating loop; green, C2 domain; and purple, disordered C-terminal tail (C-tail). *Bottom*: S4 sequence alignment among VSP orthologs. Dr; *Danio rerio*, Hs; *Homo sapiens*. R1 to R4 denote positively charged residues. Magenta, conserved isoleucine and phenylalanine. (*B*) Representative GIRK2d channel traces in oocytes expressing WT, I233Q, and F234Y Ci-VSP. The pulse protocol (*Left*) composed of a 50-ms ramp, 50-ms test step, and 300-ms depolarization was repeated 21 times, and all traces recorded during the test pulse (surrounded by a dotted square in the *Left panel*) are superimposed. Dotted lines indicate zero current level. (*C*) Time course of GIRK2d current in oocytes expressing WT, I233Q, and F234Y mutants. The current amplitudes at the end of the test pulse were normalized to that in the first trace, and mean normalized amplitudes were plotted against time. Data are shown as mean ± SD; *n* = 22, 8, and 7 for WT, I233Q, and F234Y, respectively. The rate constant of the current decay determined by fitting it with a single exponential function was taken as the phosphatase activity (see also *SI Appendix*, Fig. S1). (*D*) Representative TMRM fluorescence traces of G214C*, I233Q/G214C*, and F234Y/G214C* in response to depolarizing pulses (*Top*) to potentials indicated by colors. (*E*) *Top*: F-V curves for G214C*, I233Q/G214C*, and F234Y/G214C*; mean ± SD (*n* = 13, 7, and 8, respectively). *Bottom*: Phosphatase activity of WT, I233Q, and F234Y mutants at different potentials; mean ± SD (*n* ≥ 5 at each potential). The fluorescence values at the end of depolarization were normalized to that at 200 mV. Curves are Boltzmann fits, and values of (V$_{1/2}$, z) are (69.3 ± 0.7 mV, 1.0), (103.7 ± 0.6 mV, 1.0), and (80.5 ± 1.1 mV, 0.7) for G214C*, I233Q/G214C*, and F234Y/G214C*, respectively. Dotted arrows in the *Bottom panel* indicate the phosphatase activity at V$_{1/2}$ of the F-V curve. (*F*) Plots for phosphatase activities at 50 mV against the hydrophobicity of the amino acid side chain at I233 (*Left*) and F234 (*Right*). Data are shown as mean ± SD; *n* ≥ 6. An asterisk indicates the original amino acid residue, and letters indicate the substituted amino acid. Black dotted line in the *Left* panel represents phosphatase activity equal to 0.01. Red dotted lines are regression lines. R^2, coefficient of determination.

S4 and the neighboring linker moves as a single α helix and approaches the hydrophobic spine. We propose that the hydrophobic spine operates as a hub for electrochemical coupling between the voltage-induced motion of the VSD and the PTEN-like enzyme.

Results and Discussion

The Hydrophobicity of the C-terminal End of S4 Is Essential for Phosphatase Activity in Ci-VSP. Amino acid sequence alignment of VSP homologs showed that isoleucine and phenylalanine at the C-terminal end of S4, downstream from the fourth arginine (R4), are highly conserved (Fig. 1*A*). To investigate the function of this region of S4, residues I233 and F234 of Ci-VSP were respectively substituted with the hydrophilic amino acids glutamine and tyrosine, which have side chains similar in length to those of the original amino acids. Voltage-dependent phosphatase activities of the mutants were compared with those of the wild-type (WT) using a PI(4,5)P$_2$-sensitive inwardly rectifying K$^+$ (K$_{ir}$) channel (GIRK2d) as the sensor for PI(4,5)P$_2$ in *Xenopus* oocytes (21, 23). By fitting the decay of the inward current elicited by a test pulse to −120 mV upon

repeated depolarization with a single exponential function, its rate constant was taken as the phosphatase activity in this study (*SI Appendix*, Fig. S1 *A* and *B*). When WT Ci-VSP was coexpressed, the current decreased rapidly upon repeated depolarization to 50 mV (Fig. 1 *B* and *C*). By contrast, the I233Q mutant induced little current decrease, and the F234Y mutant induced only a gradual decrease in current amplitude (Fig. 1 *B* and *C* and *SI Appendix*, Fig. S1*C*).

To characterize the VSD motion in the two mutants, we performed VCF (24). A thiol reactive fluorescent dye, tetramethyrhodamine-6-maleimide (TMRM), was attached to a cysteine residue substituted at G214, which was situated at the external top of S4 (14, 15, 21, 25) (G214C; Fig. 1 *D*, *Inset*). G214C-TMRM (G214C*) in Ci-VSP has been shown to exhibit robust fluorescence changes associated with voltage-dependent VSD motion (25). Both I233Q/G214C* and F234Y/G214C* showed robust voltage-induced changes in fluorescence with a rightward shift of the fluorescence–voltage (F-V) relationship compared to G214C* (Fig. 1 *D* and *E*). The voltage V$_{1/2}$, which gives half of the maximum change of fluorescence, was shifted rightward by 34.4 mV and 11.2 mV in I233Q/G214C* and F234Y/G214C*, respectively. When the phosphatase activities were measured at

different membrane potentials (0 mV to 175 mV by 25-mV increments), the activities of both the I233Q and F234Y mutants at the $V_{1/2}$ of the F-V curve were remarkably smaller than that of the WT (Fig. 1 *E, Bottom*). This indicates that the reduction in voltage-dependent phosphatase activity of the two mutants cannot be simply explained by a shift of the voltage dependence of the VSD motion.

Residues I233 and F234 were then individually substituted with various amino acids, and their phosphatase activities were compared with that of WT, I233Q, and F234Y. When the phosphatase activities of the mutants measured at 50 mV were plotted against the Kyte-Doolittle hydrophobicity scale (26), they correlated with the hydrophobicity of the side chain, but not with the side chain van der Waals volume (27) (Fig. 1*F* and *SI Appendix*, Fig. S2*B*). We also measured sensing currents (*SI Appendix*, Fig. S2 *C, Inset*) derived from the movements of positively charged amino acids within S4, which correspond to the gating currents of VGICs (8). Plots of the moving charges of the off sensing currents (Q_{OFF}s) against membrane potential (*SI Appendix*, Figs. S2*C* and S8 and Table S1) showed some voltage shifts. We compared the phosphatase activities of the mutants with such a voltage shift taken into account: Among a set of data of phosphatase activity from individual cells, the activity measured at a voltage (among eight steps from 0 mV to 175 mV by 25-mV increments) nearest to that of 50 plus difference of the $V_{1/2}$ (Q_{OFF}), where Q_{OFF} reaches half the maximum value, between WT and a mutant [approximately 50 + $\Delta V_{1/2}$ (Q_{OFF}) (mV)], was plotted similarly to Fig. 1*F* and *SI Appendix*, Fig. S2*B* (*SI Appendix*, Figs. S3 and S4). There was yet a clear correlation between the phosphatase activity and the hydrophobicity of the side chain at both I233 and F234 (R^2 = 0.638 and 0.564 for I233 and F234, respectively; *SI Appendix*, Figs. S3*B* and S4*B*). Four other hydrophobic residues in S4 upstream from R4 (L225, V228, L230, and A231) were similarly studied. In contrast to I233 and F234, several hydrophilic substitutions of these residues did not decrease phosphatase activity (*SI Appendix*, Figs. S5, S7, S8 and Table S1).

We then studied three residues (Y235, S236, and H237) downstream from F234. Replacement of each residue in this region with a hydrophobic residue resulted in an increase in phosphatase activity (*SI Appendix*, Figs. S6 and S7) that was accompanied by a leftward shift of the $V_{1/2}$ (Q_{OFF}) (*SI Appendix*, Figs. S6*C* and S8 and Table S1). Phosphatase activity at 50 mV showed a less clear but significant correlation with the degree of hydrophobicity of the side chains of these three residues compared with I233 and F234 (*SI Appendix*, Fig. S6*B*). However, in S236 and H237, this correlation can be accounted for mainly by the leftward shift of the voltage-dependence of the VSD motion (*SI Appendix*, Fig. S6 *D* and *E*).

VSD-CCR Coupling Is Altered by Mutation of I233 and F234. To determine whether coupling states between the VSD and the CCR of Ci-VSP are altered by mutations at I233 and F234, we measured fluorescence changes in TMRM attached to a substituted cysteine residue at Q208 in the middle of the S3-S4 extracellular loop (Q208C; Fig. 2 *A, Inset*). Voltage-dependent fluorescence changes in Q208C-TMRM (Q208C*) reportedly contain a component that mediates retrograde signals from the CCR to the VSD (14, 15, 25) and can thus serve as a sensitive indicator of alterations of that coupling. As previously reported, Q208C* in the WT showed a complex triphasic fluorescence change upon membrane depolarization (Fig. 2*B*): first, a small increase (Fig. 2*A*, light gray and gray traces) at voltages from the holding potential of −60 mV to 20 mV; second, a large

decrease (Fig. 2*A*, purple and blue traces) at voltages between 20 mV and 100 mV; and third, an increase (Fig. 2*A*, green and red traces) at voltages more positive than 100 mV (14, 15, 25). The positive third component has been shown to reflect S4 motion and to correlate with VSD-CCR coupling (15). I233Q mutation shifted the negative second component toward more positive voltages with an expansion of the first component to a wider range of voltages. The positive third component was not observed, even at 200 mV. The F234Y mutation did not affect the first component but enhanced the second component while suppressing the third component (Fig. 2 *A* and *B*). These results suggest that VSD-CCR coupling was diminished in the I233Q and F234Y mutants.

To further investigate the effects of mutations within the C-terminal end of S4 on the CCR, we used Anap to assess voltage-dependent conformational rearrangements within the CCR (28). K555 is located at the membrane side of the C2 domain, near the PD, and indirectly interacts with the substrate via several hydrogen bonds (20). In earlier studies, we observed that Anap incorporated at K555 exhibited a biphasic fluorescence change at a bandwidth of 460 to 510 nm: an initial fast decrease at 0 mV to 100 mV and a large increase at higher membrane potentials (17, 21) (Fig. 2 *C* and *D*). The second increasing component reflects voltage-dependent conformational rearrangement within the CCR linked to S4 motion, which induces robust phosphatase activity and indicates a tight correlation with VSD-CCR coupling (21).

I233Q and F234Y mutations were individually introduced in K555Anap Ci-VSP, and their effects on Anap fluorescence changes were examined. Both constructs were robustly expressed on the cell surface as evidenced by voltage-evoked sensing currents (*SI Appendix*, Fig. S9). Oocytes expressing I233Q/K555Anap exhibited only a fluorescence decrease similar to the first component of K555Anap at membrane potentials greater than 100 mV, and the second increasing component was lost (Fig. 2 *C* and *D*). F234Y mutation did not affect the first component but reduced the amplitude of the fluorescence change in the second increasing component (Fig. 2 *C* and *D*). These findings indicate that hydrophilic substitution within the C-terminal end of S4 affects VSD-CCR coupling, attenuating voltage-dependent fluorescence changes in K555Anap at higher membrane potentials. Taken together, these findings indicate that two residues at the C-terminal end of S4, I233 and F234, play critical roles in VSD-CCR coupling.

S4 and Its C-terminal Proximal Linker Region Move as a Single Helix. To study voltage-dependent local structural rearrangements of I233 and F234, we genetically incorporated Anap on I233 or F234. At a bandwidth of 460 to 510 nm, both I233Anap and F234Anap showed voltage-dependent decreases in fluorescence upon membrane depolarization to more than 0 mV (Fig. 3 *A–D*). F234Anap also showed a decrease of fluorescence at a bandwidth of 420 to 460 nm (*SI Appendix*, Fig. S10 *E* and *F*). I233Anap exhibited a more complex pattern of fluorescence changes than F234Anap at the 420- to 460-nm bandwidth: There was an initial fluorescence increase at membrane potentials less than 100 mV and a second slower component with a fluorescence decrease at higher membrane potentials (*SI Appendix*, Fig. S10 *C* and *D*).

Given that S4 moves upward upon activation of the VSD, we hypothesized that these fluorescence changes in I233Anap and F234Anap result from interactions with other transmembrane helices. It has been reported that aromatic amino acids quench various types of fluorophores through electron transfer (29, 30). With that in mind, we focused on W182 within S3 at the border between the intracellular side of the membrane and
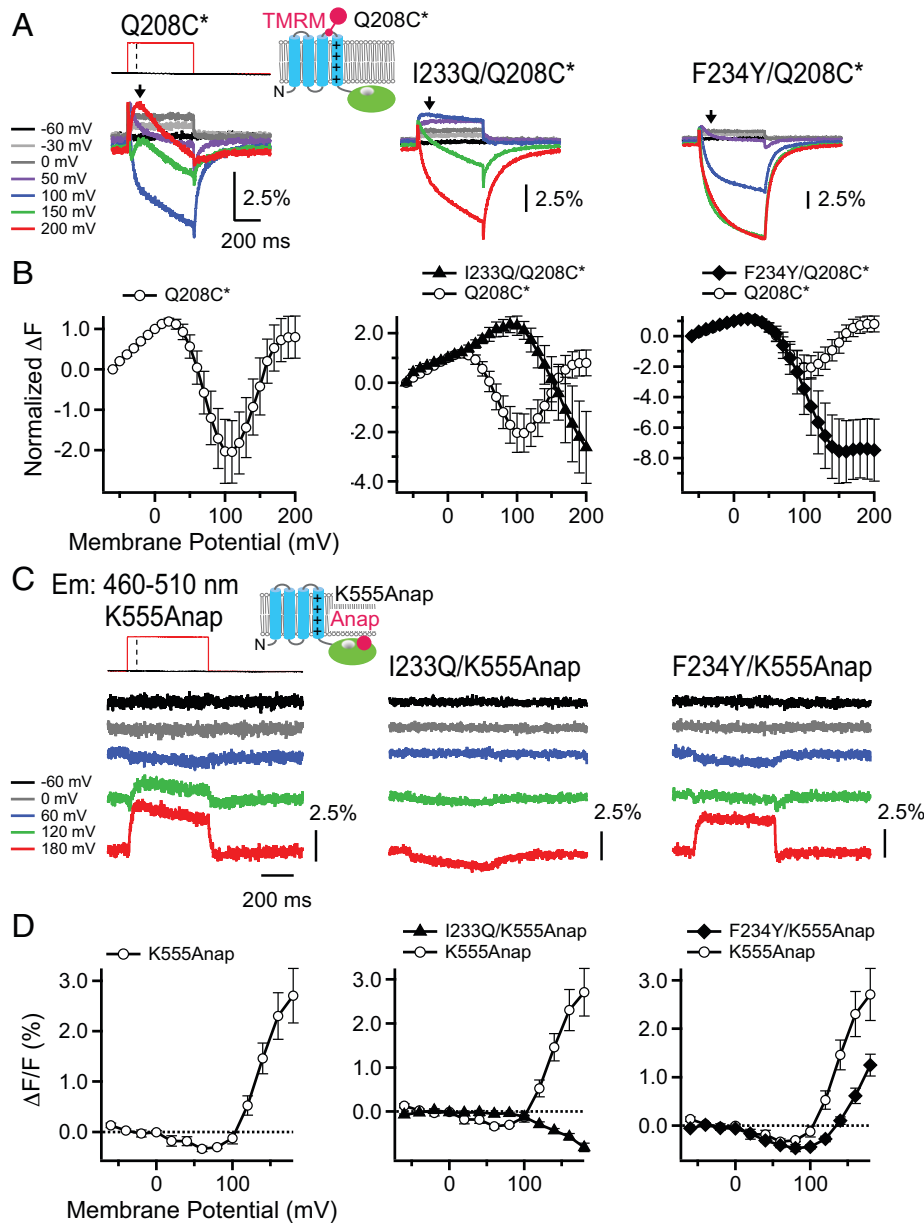
Fig. 2. Fluorometric analysis of voltage-driven conformational changes in S4 and the CCR with mutations at the C-terminal end of S4. (A) Representative TMRM fluorescence traces of Q208C* (cartoon Inset), I233Q/Q208C*, and F234Y/Q208C* in response to depolarizing pulses (Top) to potentials indicated by colors. (B) F-V curves for Q208C* (Left), I233Q/Q208C* (Center), and F234Y/Q208C* (Right). The fluorescence values measured at arrows in A (average values between 200 ms and 210 ms) were normalized to that at 0 mV. Data are shown as mean ± SD; n = 10, 6, and 8 for Q208C*, I233Q/Q208C*, and F234Y/Q208C*, respectively. (C) Representative fluorescence traces of K555Anap (cartoon Inset), I233Q/K555Anap, and F234Y/K555Anap during depolarization (Top) to potentials indicated by colors. The fluorescence was detected using a 460- to 510-nm band-pass emission filter (Em). (D) F-V curves for K555Anap (Left), I233Q/K555Anap (Center), and F234Y/K555Anap (Right). The fluorescence values before depolarization were subtracted from those at the beginning of depolarization (ΔF), and then ΔF was normalized to that at −60 mV. Data are shown as mean ± SEM; n = 3, 10, and 12 for K555Anap, I233Q/K555Anap, and F234Y/K555Anap, respectively.

the cytoplasm. We first tested the effect of tryptophan on Anap in solution. Spectral measurements indicated that Anap fluorescence was quenched by tryptophan and that the effect was concentration-dependent (SI Appendix, Fig. S10 A and B). We then examined the effects of W182A mutation on changes in the fluorescence of I233Anap and F234Anap elicited by membrane depolarization. At both the 460- to 510-nm and 420- to 460-nm bandwidths, the decrease in W182A/F234Anap fluorescence was diminished at membrane potentials greater than 60 mV (Fig. 3 C and D and SI Appendix, Fig. S10 E and F) with no change in the Q_{OFF}-voltage (Q_{OFF}-V) relationship (SI Appendix, Fig. S10I). This is consistent with the idea that F234Anap fluorescence was quenched by interaction with W182. W182A mutation also diminished the decrease in I233Anap fluorescence within the 460- to 510-nm bandwidth (Fig. 3 A and B). Within the 420- to 460-nm bandwidth, W182A mutation eliminated the second (decreasing) component of I233Anap fluorescence, but it did not affect the first (increasing) component (SI Appendix, Fig. S10 C and D). These results suggest that I233Anap florescence contains a

component that reflects quenching by W182. Collectively, these findings suggest the C-terminal end of S4 comes close to the cytoplasmic end of S3 upon membrane depolarization.

We also examined the voltage-dependent motion of H237, which is in the proximal region of the VSD-PD linker. We found that H237Anap exhibited a large fluorescence change in response to membrane depolarization, in particular within the 460- to 510-nm bandwidth (Fig. 3 E and F). Notably, changes in H237Anap fluorescence were reciprocal between the two bandwidths: a decrease within the 460- to 510-nm bandwidth (Fig. 3 E and F) but an increase in the 420- to 460-nm bandwidth (SI Appendix, Fig. S10 G and H). Like I233Anap, H237Anap fluorescence within the 420- to 460-nm bandwidth exhibited a biphasic change (SI Appendix, Fig. S10 G and H): an early increase at voltages up to 60 mV and a later marked decrease at voltages greater than 80 mV. Introduction of the W182A mutation remarkably suppressed the depolarization-evoked decrease in H237Anap fluorescence within both the 460- to 510-nm (Fig. 3 E and F) and the 420- to 460-nm bandwidths (SI Appendix, Fig. S10 G and H). In the latter, H237Anap fluorescence from the
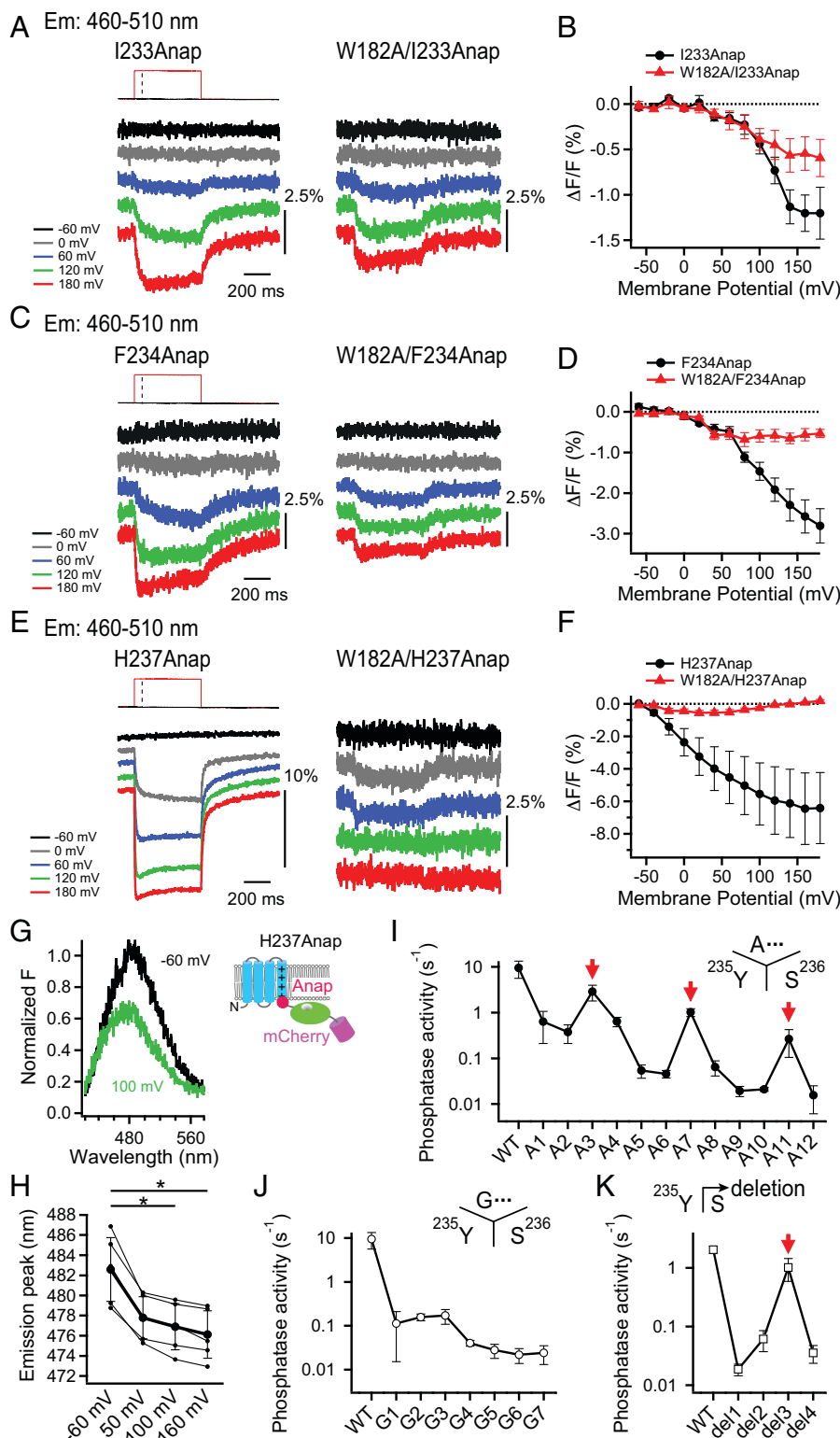
Fig. 3. Analysis of voltage-driven changes in the fluorescence of Anap introduced at I233, F234, and H237 and the helical nature of the VSD-PD linker. (*A*, *C*, and *E*) Representative fluorescence traces of I233Anap (*A*), F234Anap (*C*), and H237Anap (*E*) with or without W182A mutation during depolarization (*Top*) to potentials indicated by colors. The fluorescence was detected using a 460- to 510-nm band-pass emission filter (Em). W182A mutation suppressed fluorescence decrease during membrane depolarization. (*B*, *D*, and *F*) F-V curves for I233Anap (*B*), F234Anap (*D*), and H237Anap (*F*). Red lines show the plots from W182A mutants. The fluorescence values before depolarization were subtracted from those at the beginning of depolarization (ΔF), and then ΔF was normalized to that at −60 mV. Data are shown as mean ± SEM; $n = 7$ for both I233Anap and W182A/I233Anap, $n = 6$ for both F234Anap and W182A/F234Anap, $n = 4$ for H237Anap, and $n = 3$ for W182A/H237Anap. (*G*) Representative Anap emission spectra at −60 mV (black) and 100 mV (green) for H237Anap Ci-VSP fused with a C-terminal mCherry (cartoon is shown in *Inset*). Spectra were recorded from the same oocyte and normalized to the spectrum at −60 mV. (*H*) Anap emission peak values of H237Anap at four indicated membrane potential levels. Thin lines, individual oocytes ($n = 5$); thick line, mean ± SD across oocytes. *$P < 0.05$, Tukey-Kramer test. (*I–K*) Summary of phosphatase activities at 50 mV for WT and mutants with amino acid insertion (*I* and *J*) or deletion (*K*). Data are shown as mean ± SD; $n \geq 3$. Phosphatase activity gradually decreased in accordance with an increase in the number of inserted alanines and deleted residues; however, it partially recovered at A3, A7, and A11 (red arrows in *I*) and del3 (red arrow in *K*). Glycine inserted mutants did not show such a recovery (see also *SI Appendix,* Fig. S14).

W182A mutant was larger as the membrane potential was more positive, in contrast to the biphasic pattern in the construct without this mutation, which showed diminished fluorescence at higher potentials (*SI Appendix,* Fig. S10*H*). When oocytes expressing H237Anap were hyperpolarized from a holding potential of −20 mV, the direction of the fluorescence changes was opposite to those elicited with depolarizing pulses (*SI Appendix,* Fig. S11*C* versus Fig. 3*E* in the 460- to 510-nm bandwidth; *SI Appendix,* Fig. S11*A* versus *SI Appendix,* Fig. S10*G* in

the 420- to 460-nm bandwidth). The fluorescence changes observed upon hyperpolarization were also greatly repressed in the W182A mutant (*SI Appendix,* Fig. S11). These findings suggest that H237 interacts with W182 in a voltage-dependent manner.

Given that the Anap emission spectrum is known to be shifted toward shorter wavelengths with exposure to a more hydrophobic environment (28), reciprocal changes in H237Anap fluorescence between the two bandwidths might suggest that the hydrophobicity of the environment surrounding the Anap on
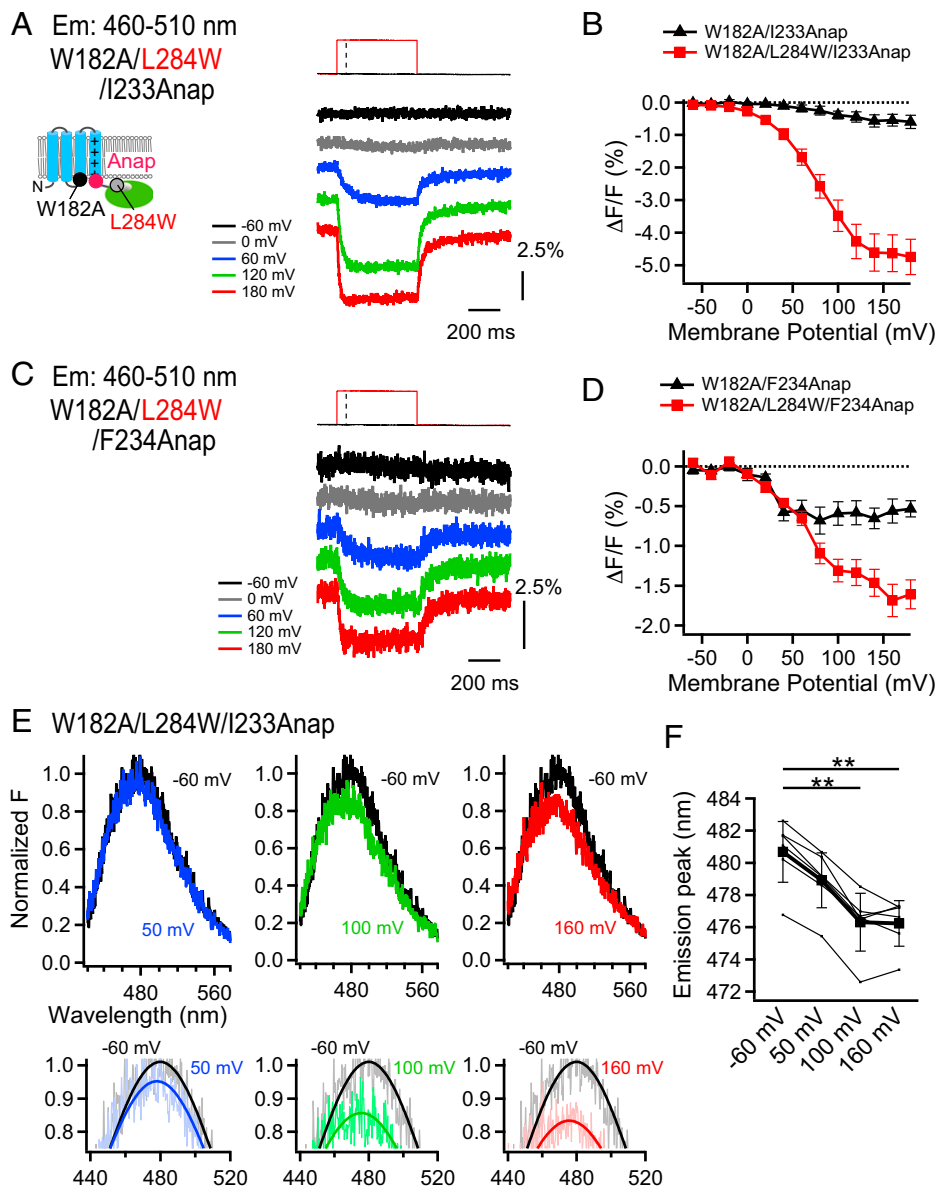
Fig. 4. Interaction of the C-terminal end of S4 with the hydrophobic spine revealed by Anap fluorescence. (*A* and *C*) Representative Anap fluorescence traces of W182A/L284W/I233Anap (*A*) and W182A/L284W/F234Anap (*C*) in response to depolarizing steps (*Top*) to indicated potential levels. The fluorescence was detected using a 460- to 510-nm band-pass emission filter (Em). (*A*, *Inset*) Schematics of Ci-VSP with Anap incorporated in I233 or F234. W182 on S3 and L284 in the hydrophobic spine were mutated to Ala and Trp, respectively. (*B* and *D*) F-V curves for W182A/L284W/I233Anap (*B*) and W182A/L284W/F234Anap (*D*). The fluorescence values before depolarization were subtracted from those at the beginning of depolarization (ΔF), and then ΔF was normalized to that at −60 mV. Data are shown as mean ± SEM; $n = 7$ and 9 for W182A/L284W/I233Anap and W182A/L284W/F234Anap, respectively. (*E*) Representative Anap emission spectra at −60 mV (black), 50 mV (blue), 100 mV (green), and 160 mV (red) for W182A/L284W/I233Anap. The spectra at −60, 50, 100, and 160 mV were recorded from the same oocyte and normalized to the spectrum at −60 mV. *Lower:* Panels are magnification of the spectra shown in *Upper panels*. Curves are Gaussian fits. (*F*) Changes in Anap emission peak values of W182A/L284W/I233Anap in response to membrane depolarization. Thin lines, individual oocytes ($n = 6$); thick line, mean ± SD across oocytes. **$P < 0.01$, Tukey-Kramer test.

H237 is altered by changes in membrane potential. Therefore, by using an imaging system composed of a spectrograph connected to a cooled, electron-multiplying charge-coupled device camera (see *Materials and Methods*), the Anap emission spectrum was recorded from H237Anap under two-electrode voltage clamp (TEVC) (*SI Appendix*, Fig. S12 *A* and *B*). We observed that a 6.5 ± 1.4 nm shift in the H237Anap emission peak to shorter wavelengths accompanied the decrease in fluorescence intensity elicited by membrane depolarization to 160 mV ($n = 5$; Fig. 3 *G* and *H* and *SI Appendix*, Fig. S12 *C* and *D*). When the membrane was hyperpolarized, the H237Anap emission peak was shifted by 1.7 ± 0.2 nm in the opposite direction ($n = 4$; *SI Appendix*, Fig. S12 *F–H*). The peak of emission spectrum was not shifted when the recording was similarly performed with several negative controls, including unincorporated Anap in cells injected Ci-VSP complementary RNAs (cRNAs) lacking an *amber* nonsense codon (TAG) (*SI Appendix*, Fig. S13 *C* and *D*); endogenous fluorescence from the animal pole in uninjected oocytes, which has an emission peak similar to that of Anap (31) (*SI Appendix*, Fig. S13 *A* and *B*); and mCherry fused to the C-terminal of Ci-VSP for verification of cell surface expression (*SI Appendix*, Figs. S12*E* and S13*E*). Based on these findings, we suggest that W182 interacts with

Anap incorporated at H237 via at least two mechanisms during S4 motion: fluorescence quenching and changes in the hydrophobicity of the local environment. Although understanding of the physicochemical mechanisms underlying the complex changes in H237Anap fluorescence still needs further detailed investigation, these findings support the idea that H237 approaches W182 with the upward motion of the VSD during depolarization and moves away from W182 with the downward motion of the VSD during hyperpolarization. Within the available structures of the Ci-VSP VSD in an activated state, H237 is located at the interface of the plasma membrane and the cytoplasm (32). However, our findings suggest that S4 must move farther upward than in these structures, and H237, which is situated within the VSD-PD linker region, is also incorporated into the membrane upon membrane depolarization.

Based on the observations that I233, F234, and H237 similarly approach W182, we hypothesized that S4 and the proximal part of the VSD-PD linker move as a solid helical structure. To test this idea, we inserted various numbers of alanines at the C-terminal end of S4 (*SI Appendix*, Fig. S14*A*). When one or two alanines were inserted between Y235 and S236 (A1 or A2, respectively), phosphatase activity was diminished compared to the WT.
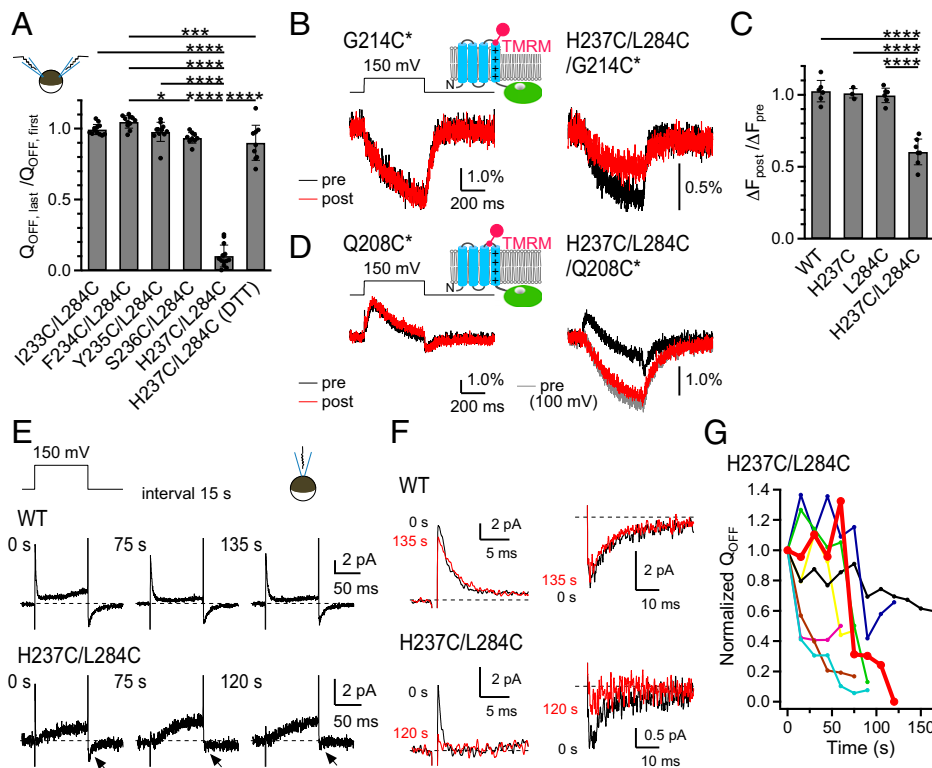
Fig. 5. Voltage-dependent disulfide locking with a pair of cysteines in the C-terminal end of S4 and the hydrophobic spine. (*A*) Summary of a decrease in Q_{OFF} by a disulfide locking with a pair of cysteines in I233-H237 and L284 during a repetitive sensing current measurement under TEVC. $Q_{OFF, first}$ means Q_{OFF} at 0 s, and $Q_{OFF, last}$ means Q_{OFF} at 210 s except for H237C/L284C. $Q_{OFF, last}$ in H237C/L284C and DTT-pretreated H237C/L284C was defined as Q_{OFF} at the last point and at 435 s, respectively. Bars are means ± SD; $n = 12, 11, 11, 9, 13$, and 9 for I233C/L284C, F234C/L284C, Y235C/L284C, S236C/L284C, H237C/L284C, and H237C/L284C (DTT), respectively; *$P <$ 0.05, ***$P <$ 0.001, ****$P <$ 0.0001, Tukey-Kramer test. (*B* and *D*) Representative TMRM fluorescence traces of G214C* (*B*) and Q208C* (*D*) with or without H237C/L284C mutation in response to step to 150 mV. The traces recorded before (black, pre) and after (red, post) a repetitive sensing current measurement were superimposed. For comparison, the trace of H237C/L284C/Q208C* recorded at 100 mV is shown (gray). Six and seven oocytes from more than two batches were recorded for Q208C* and H237C/L284C/Q208C*, respectively, and reproducible results were obtained. (*C*) Summary of G214C* fluorescence change after a repetitive sensing current measurement. Bars are means ± SD; $n = 6, 3, 6$, and 7 for G214C*, H237C/G214C*, L284C/G214C*, and H237C/L284C/G214C*, respectively; ****$P <$ 0.0001, Tukey-Kramer

test. (*E*) Representative traces of WT and H237C/L284C recorded in the on-cell patch configuration. Sensing currents were evoked repeatedly (*Top*), and timing of recording is shown at each trace. Off sensing currents of H237C/L284C are indicated by black arrows. (*F*) On (*Left*) and off (*Right*) sensing currents of WT and H237C/L284C recorded at 0 s (black) and 135 s (red, WT) or 120 s (red, H237C/L284C) were superimposed at an enlarged scale. In *E* and *F*, dotted lines indicate zero current level. (*G*) The time course of normalized Q_{OFF} of eight oocytes expressing H237C/L284C. Red line indicates the result shown in E. In all oocytes, decrease in Q_{OFF} started within 90 s.

However, insertion of three alanines (A3) led to partial recovery of phosphatase activity (Fig. 3*I* and *SI Appendix*, Fig. S14*B*). As the number of inserted alanines was further increased, phosphatase activity continued to weaken; however, partial recovery was periodically observed with every four inserted alanines (Fig. 3*I*, red arrows). We also inserted various numbers of glycines at the same site. Insertion of a single glycine (G1) was sufficient to suppress phosphatase activity (Fig. 3*J* and *SI Appendix*, Fig. S14*B*). With insertion of multiple glycines, we did not detect the periodic recovery we saw with alanine (Fig. 3*J* and *SI Appendix*, Fig. S14*B*). These results suggest that a solid helical structure in the C-terminal proximal region of S4 is important for VSD-CCR coupling. To gain further insight into the structure of the C-terminal proximal region of S4, we then measured the phosphatase activity of mutants in which one to four residues were deleted from S236 (*SI Appendix*, Fig. S14*C*). Deletion of three residues (del3) partially recovered phosphatase activity, while deletion of one, two, or four residues repressed activity (Fig. 3*K* and *SI Appendix*, Fig. S14*D*), showing periodicity similar to that observed with insertion of multiple alanines (A1 to A4). Collectively, these results support that a single α helical structure is formed from S4 to the initial part of the VSD-PD linker.

The VSD Interacts with the Hydrophobic Spine of the CCR. The hydrophobic spine situated at the interface between the plasma membrane and the distal end of the PD (L284 and F285 in Ci-VSP) plays a critical role in VSD-CCR coupling (21, 22). Because hydrophobicity at both the C-terminal end of S4 and the hydrophobic spine plays a critical role in VSD-CCR coupling, we hypothesized that the C-terminal end of S4 directly interacts with the hydrophobic spine.

Having found that a native tryptophan influences Anap fluorescence upon voltage-dependent conformational rearrangement

of Ci-VSP (Fig. 3 and *SI Appendix*, Figs. S10–S12), we used this feature of tryptophan to examine the region in its physical proximity within the Ci-VSP polypeptide during voltage-dependent conformational rearrangements. We substituted a tryptophan at L284 and incorporated Anap at I233 or F234 within the W182A mutant (Fig. 4 *A*, *Inset*). In oocytes expressing W182A/L284W/I233Anap or W182A/L284W/F234Anap, depolarizing pulses elicited a clear fluorescence decrease in the 460- to 510-nm bandwidth (Fig. 4 *A–D*) with a small leftward shift in the Q_{OFF}-V curve compared with mutants without L284W (*SI Appendix*, Fig. S15*E*). In the 420- to 460-nm bandwidth, W182A/L284W/F234Anap exhibited a fluorescence decrease at voltages greater than 60 mV (*SI Appendix*, Fig. S15 *C* and *D*). Changes in F234Anap fluorescence elicited by introduction of tryptophan to L284 observed at over 60 mV in both bandwidths are consistent with fluorescence quenching by tryptophan. On the other hand, W182A/L284W/I233Anap exhibited a biphasic fluorescence change like that seen with I233Anap (*SI Appendix*, Fig. S15 *A* and *B*), which suggests a spectrum shift toward shorter wavelengths.

To better understand how introduction of a tryptophan at L284 changed the Anap signal at I233, we measured the emission spectrum of the W182A/L284W/I233Anap mutant as we did with H237Anap (Fig. 3 *G* and *H* and *SI Appendix*, Fig. S12). The emission peak for I233Anap was gradually shifted to shorter wavelengths as the membrane potential became more positive (Fig. 4*E*). For instance, the emission peak at 160 mV was shifted by 4.5 ± 0.9 nm ($n = 6$; Fig. 4*F*) compared to that at −60 mV. This suggests that the effect of tryptophan at residue 284 on the fluorescence recorded from Anap at residue 233 upon a change in membrane potential reflects its hydrophobic nature. Although tryptophan at residue 284 appears to alter Anap fluorescence at residues 233 and 234 through
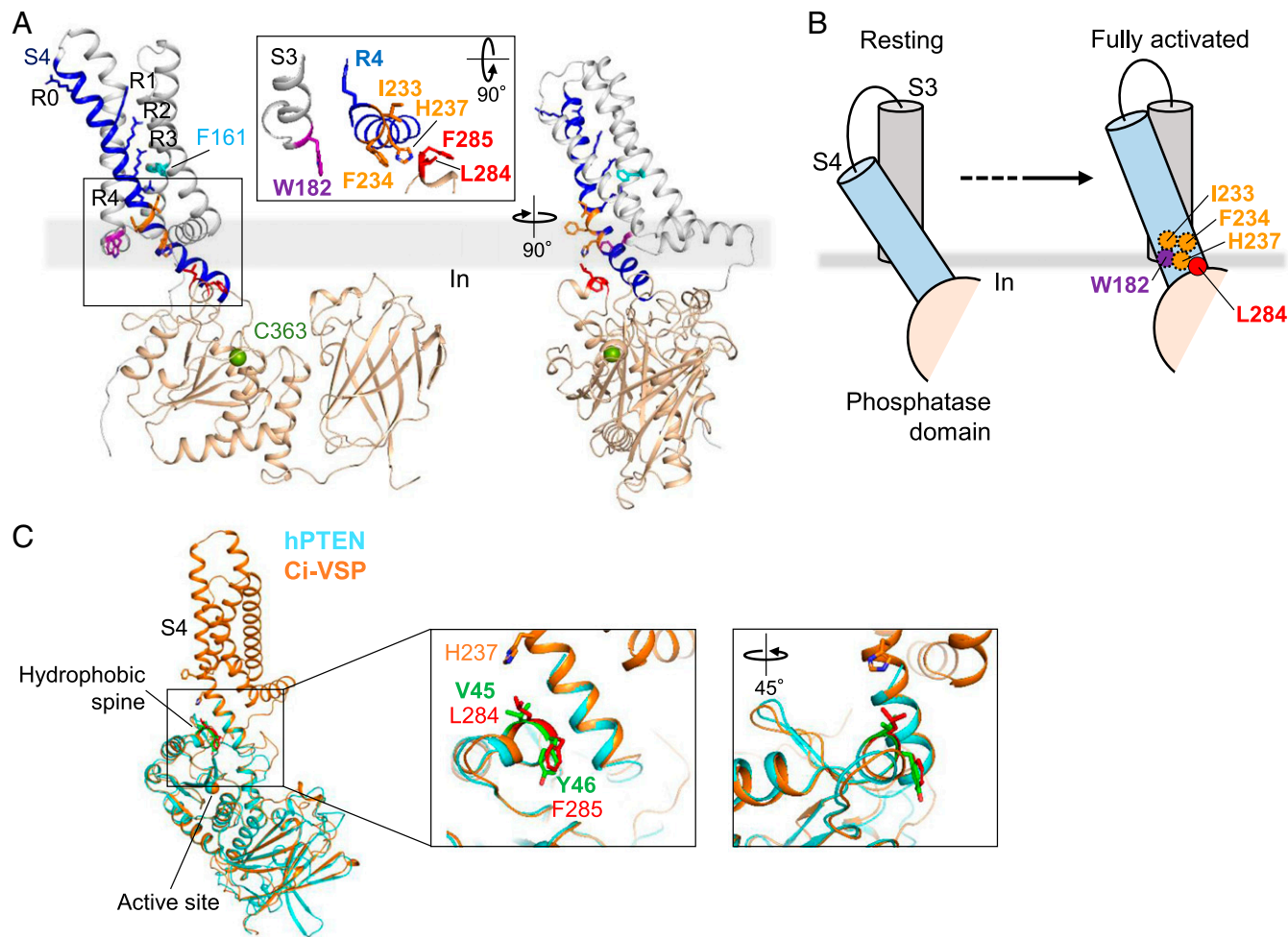
Fig. 6. Structural and proposed models of VSD-CCR coupling mechanism in Ci-VSP. (*A*) Ribbon diagrams of the full-length Ci-VSP model. The bold gray horizontal line represents the cytoplasmic side of the plasma membrane. The S4-linker helix is colored blue. Side chains are shown as sticks for the positive charges on S4: R217 (R0), R223 (R1), R226 (R2), R229 (R3), and R232 (R4) (blue); for the hydrophobic gasket: F161 (light blue); for I233, F234, and H237 (orange); for W182 (magenta); and for the hydrophobic spine: L284 and F285 (red). C$_\alpha$ atom of the active site (C363) is shown as a sphere (green). *Inset*: Close-up top view of the region surrounded with a black box. (*B*) Schematic model for coupling in Ci-VSP. S3, S4, and the initial part of the PD are shown for clarity. The bold gray horizontal line indicates the cytoplasmic side of the plasma membrane. Dotted circles indicate that these four residues might be located behind S4 from this viewpoint. (*C*) Superposition of structural models of human PTEN (hPTEN, cyan) and Ci-VSP (orange) predicted using ColabFold (see *Materials and Methods*). The hydrophobic spine of both PTEN (V45 and Y46) and VSP (L284 and F285) is shown as a stick and colored green and red, respectively. *Insets*: Close-up views of the hydrophobic spine, the N-terminal helix of PTEN, and the VSD-PD linker helix surrounded with a black box.

different mechanisms, the results support the idea that both I233 and F234 interact with L284.

To confirm that the C-terminal end of S4 directly interacts with the hydrophobic spine, a disulfide-locking test of the physical proximity of the two sites was performed by introducing two cysteines. This entails forming a disulfide bond between an engineered pair of cysteines with a C$_\alpha$-C$_\alpha$ distance of ≤15 Å and a pseudodihedral angle of ≤35° (33). It is expected that if the C-terminal end of S4 is locked near the hydrophobic spine by the formation of the disulfide bond, the voltage-dependent motion of S4 will be restricted. We predicted that the two cysteine residues would be in closest proximity at 150 mV, since the fluorescence signals from I233Anap and F234Anap in the W182A/L284W mutant were saturated at that voltage (Fig. 4 *A–D*). Oocytes were repeatedly depolarized to 150 mV. Neither the I233C/L284C nor the F234C/L284C mutant showed any change in sensing current amplitude or Q$_{OFF}$ during repeated measurements (Fig. 5*A* and *SI Appendix*, Fig. S16 *A and B*). However, an H237C/L284C mutant exhibited a gradual decrease in sensing current amplitude and Q$_{OFF}$ within 210 s, and Q$_{OFF}$ decreased to 10.1 ± 7.6% (*n* = 13; Fig. 5*A* and *SI Appendix*, Fig. S16 *C and D*). By contrast, sensing currents recorded from

oocytes expressing the Y235C/L284C or S236C/L284C mutant were unchanged (Fig. 5*A* and *SI Appendix*, Fig. S16 *A and B*). Likewise, sensing currents from cells expressing the WT or a single-cysteine mutant (H237C or L284C) were also unchanged (*SI Appendix*, Fig. S16 *C, E, I, and J*). In addition, preincubation of the cells with the reducing agent dithiothreitol (DTT) suppressed the decrease in Q$_{OFF}$ (Fig. 5*A* and *SI Appendix*, Fig. S16 *F and G*), verifying that a disulfide bond was formed between H237 and L284. The decrease in Q$_{OFF}$ in H237C/L284C was milder and slower when the depolarizing step was smaller than 150 mV (*SI Appendix*, Fig. S16*H*). By contrast, H237C/F285C showed no changes in the sensing current during repetitive measurements (*SI Appendix*, Fig. S16 *K and L*). These results indicate that the translocation of H237 caused by the upward motion of S4 induced by membrane depolarization brings it into close proximity of L284.

Disulfide locking of S4 in H237C/L284C upon voltage-induced S4 motion was further assessed using VCF with TMRM attached to G214 (G214C*) or Q208 (Q208C*) (Fig. 5 *B* and *D*). Sensing currents and TMRM fluorescence were measured from the same oocytes. The fluorescence change at G214C* in H237C/L284C was significantly suppressed compared to the WT after the

decrease in its sensing current amplitude (Fig. 5*B*). The amplitude of the change in the G214C* signal at 150 mV in H237C/L284C was decreased to 60.3 ± 8.9% of that in the WT (n = 7; Fig. 5*C*). Both the sensing currents and G214C* signals in single-cysteine mutants (H237C and L284C) were unchanged (*SI Appendix*, Fig. S17 *A* and *B*). The Q208C* signal in the WT showed a biphasic pattern consisting of an early fluorescence increase and a later decrease during 500-ms depolarizing steps to 150 mV (Fig. 5 *D*, *Left*). In H237C/L284C, once the decrease in its sensing current amplitude was observed, the Q208C* signal showed a gradual monophasic decline during depolarization to 150 mV (Fig. 5 *D*, *Right*). This signal pattern was similar to that measured at 100 mV before the sensing current amplitude decreased (Fig. 5*D*, gray trace on *Right*). These changes in the Q208C* signal and sensing current were not observed in the WT or single-cysteine mutants (Fig. 5*D* and *SI Appendix*, Fig. S17 *C* and *D*). This demonstrates that a disulfide bond was formed between the H237C and L284C residues, which restricted S4 motion and is consistent with a decrease in the sensing current amplitude.

Oocytes expressing the H237C/L284C mutant often exhibited a large leak current at the holding potential with a decrease in sensing current amplitude probably due to acute reduction of PI(4,5)P$_2$ in the entire cells. We therefore attempted to analyze H237C/L284C sensing currents in the on-cell patch configuration, which enabled us to limit VSP activity to the patch membrane. On-cell patches in WT Ci-VSP–expressing oocytes showed clear and stable sensing currents (*SI Appendix*, Fig. S17 *E–G*). The amplitudes of the sensing currents and Q$_{OFF}$ recoded from H237C/L284C-expressing cells were decreased during repetitive measurements, whereas they were unchanged in cells expressing the WT and single-cysteine mutants (Fig. 5 *E–G* and *SI Appendix*, Fig. S17 *H–J*).

Model of the Structure and Voltage-Dependent Interactions of the VSD with the Hydrophobic Spine. To gain insight into the structural basis of VSD-CCR coupling within VSP, we developed an atomic model of Ci-VSP using ColabFold (34) (see *Materials and Methods*). After comparison of the physical relationships between the arginines in S4 and the hydrophobic gasket in S2 with those of the known activated state VSD structure (PDB 4G7V) (32), the predicted structure shown in Fig. 6*A* was considered to be a more activated conformation because the arginines in the predicted structure were about one helical turn higher than those in the known structure (*SI Appendix*, Fig. S18*A*). Similar conformation of S4 within the VSD of Ci-VSP was recently predicted as an extended activated ("Up-plus") state by molecular dynamics (MD) simulations (35). S4 and the VSD-PD linker comprise a single α helix (designated as "the S4-linker helix"), and the proximal linker segment is situated within the plasma membrane. The helix break at residue 249 is consistent with the results of an earlier study, which examined voltage-dependent phosphatase activity with a cysteine mutation in the linker (19). Notably, the C-terminal end of S4 is in close proximity to the hydrophobic spine, and the hydrophobic spine forms a short α helical structure that differs from the uncoiled loop in the available X-ray crystal structure of the CCR (20). The side chain of residue 284 faces toward S4, and the C$_\alpha$-C$_\alpha$ distance for I233-L284 and F234-L284 is 15.5 Å and 14.1 Å, respectively. The side chain of W182 is also oriented toward the C-terminal end of S4, and the C$_\alpha$-C$_\alpha$ distances from I233, F234, and H237 are all consistent with the consensus distance in which fluorescence quenching by tryptophan usually occurs (∼5 to 15 Å) (30), agreeing with the

notion that residues 233, 234, and 237 interact with residue 182 and/or 284. By contrast, the C$_\alpha$-C$_\alpha$ distance for F285-H237 is longer than that for L284-H237 (12.0 Å versus 9.8 Å), and the side chain of residue 285 does not face toward S4, unlike that of residue 284, but is oriented toward the active site. This is consistent with the failure of disulfide bond formation in the H237C/F285C mutant (*SI Appendix*, Fig. S16 *K* and *L*). In a similarly predicted full-length structure of a zebrafish ortholog, Danio rerio VSP (Dr-VSP) (*SI Appendix, Fig. S18B*), the single long α helical structure extending from S4 to the VSD-PD linker is located in close proximity to L223 and Y224 (corresponding to L284 and F285 of Ci-VSP, respectively) of the hydrophobic spine. The hydrophobic spine of Dr-VSP also directs the side chains of residues 223 and 224 toward S4 and the enzyme active site, respectively (*SI Appendix*, Fig. S18*C*).

Based on both the VSD motion and local structural rearrangements of the CCR reported by Anap incorporated at K555, we previously proposed that the CCR is activated in two steps and that the hydrophobic spine is critical for the second transition (21). We found that replacement of the hydrophobic residues at the C-terminal end of S4 with hydrophilic ones diminished the second component (Fig. 2*D*), which suggests this region contributes to the second transition of the enzyme's activation. A tryptophan introduced at residue 284 quenched F234Anap fluorescence at voltages starting from 60 to 80 mV (Fig. 4*D* and *SI Appendix*, Fig. S15*D*). Because the second component of the K555Anap fluorescence change emerged at around 80 to 100 mV (21) (Fig. 2 *D*, *Left*), we speculate that voltage-dependent interaction of the S4-linker helix with the hydrophobic spine mediates VSD-CCR coupling and regulates the later state transition for phosphatase activity. We further hypothesize the following model of the structural changes underlying VSD-CCR coupling (Fig. 6*B*): Upon membrane depolarization, residues 233 and 234 interact with the hydrophobic spine, placing a hydrophobic residue near the plasma membrane. Thereafter, the entire helix moves farther upward, which places the C-terminal end of S4 near the membrane interface of S3, which corresponds to the position of W182, and places residue 237 near the hydrophobic spine at a distance and angle suitable for cysteine cross-linking in the fully activated state. Because previous MD simulations of the isolated CCR suggest rotational and/or hinge-like motions of the hydrophobic spine, with loose binding to the bilayer (21), we hypothesize that interaction between the S4-linker helix and the hydrophobic spine, which fixes the hydrophobic spine at an appropriate location near the plasma membrane, is essential for stabilizing the structure of the CCR such that it is able to bind the substrate. Further detailed analysis will be necessary to reveal the physicochemical basis underlying interaction between the S4-linker helix and the hydrophobic spine in the future.

Implications for the Mechanisms of PTEN and Other Proteins. The hydrophobic spine structure is also conserved in PTEN, which does not have a VSD but has a disordered C-terminal regulatory region (9, 21) (Fig. 1*A*). A pioneering study of the X-ray crystal structure of human PTEN by Lee et al. (36) as well as a more recent study by Dempsey et al. (37) showed that two hydrophobic residues within the hydrophobic spine, V45 and Y46, which respectively correspond to L284 and F285 of Ci-VSP, are located near the plasma membrane. The hydrophobic spine and the neighboring residues of PTEN are hot spots of mutation in human cancer patients (38–40), and mutation at either site greatly reduces phosphatase activity (21, 41). In the same study, Dempsey et al. (37) also suggest that phosphorylation events lead to folding of the disordered C-terminal tail,

placing it in close proximity to the hydrophobic spine, which reduces catalytic activity by obstructing substrate recognition or binding. These studies highlight the critical role played by the hydrophobic spine in PTEN. Furthermore, surface exposure of hydrophobic residues near the enzyme active site are a widely distributed feature of phosphoinositide phosphatases (21) (*SI Appendix,* Fig. S19). These structures play an important role in mediating anchorage to the plasma membrane and substrate recognition and binding (42–45), suggesting that hydrophobic spine-like structures are common regulatory structures governing the catalytic activity of many phosphoinositide phosphatases.

The N-terminal region of PTEN, with remarkable sequence similarity to the C-terminal region of the VSD-PD linker of VSP, has been shown to be critical for the catalytic activity of PTEN (37, 46–49). In the recently solved structure of human PTEN (PDB 7JUL), the N-terminal region forms a short α helix (37). This helix includes amino acid residues K6 and E7, which are hot spots of mutation in human cancer patients (COSMIC database). When superimposed on the predicted structure of Ci-VSP (*SI Appendix,* Fig. S20), the position of the N-terminal helix of PTEN is near the VSD-PD linker helix of Ci-VSP. Moreover, the full-length structure of human PTEN predicted with ColabFold shows that the N-terminal helix is nearly perfectly superimposable on the VSD-PD linker helix of the predicted Ci-VSP extending from upstream of S4 (root mean squared deviation: 0.763 Å over 220 C_α carbons; Fig. 6C). Notably, the distance from the N-terminal helix to the hydrophobic spine is similar between human PTEN and Ci-VSP. These findings suggest that the N-terminal helix in PTEN is similar to the part of the VSD-PD linker in VSP that regulates phosphatase activity through interaction with the hydrophobic spine. These findings support an intriguing view that by having a single long α helix from S4 to the VSD-PD linker in VSP, the VSD hijacks the regulatory mechanisms that control phosphatase activity and involve interaction with the hydrophobic spine, which are innate to PTEN and the CCR of VSP. This view can account for the finding that voltage dependence can be imposed on PTEN through simple transfer of the VSD to PTEN (50, 51).

VSP lacks the C-terminal regulatory region found in PTEN (9, 37, 52, 53) (Fig. 1A), and VSP constructs lacking the VSD exhibit phosphoinositide phosphatase activity in vitro (8, 11, 20, 21, 54, 55). These raise an important question: How is the enzyme activity of VSP silenced at resting membrane potential? X-ray crystal structures of the isolated CCR show that the PD assumes two conformations. In one conformation, a flexible loop, which is called the gating loop and is conserved among VSPs but not in PTEN, is positioned outside of the substrate binding pocket, which widens the substrate-binding space. By contrast, in the second conformation, the gating loop is directed toward the pocket, with the E411 residue narrowing the substrate-binding space (20). These suggest that a structural change to the S4-linker helix induces conformational rearrangement of the gating loop that precludes access of the substrate to the enzyme active site (20). This suggests that upon membrane hyperpolarization, structural rearrangement of the S4-linker helix may, in addition to destabilizing the hydrophobic spine, allosterically induce conformational changes in the gating loop to silence phosphatase activity. Further analysis of the conformational rearrangements of both the VSD and the CCR will be necessary to test these ideas. In addition, further investigation of the coupling mechanisms in VSP will help to understand how, during the course of evolution, nature was able to diversify signals downstream of a VSD such that they are well suited to their specific biological contexts, which include metabolism, reproduction, and behavior.

Conclusions

Within VSP, S4 and the C-terminal–franking portion of the VSD-PD linker form a single straight helix. Upon membrane depolarization, the helix interacts with the hydrophobic spine, a membrane-bound structure within the PD, which was previously shown to be involved in the second transition of the enzyme's activation. We propose that the voltage-induced interaction between these two regions stabilizes the catalytic mode of the CCR, ensuring robust enzyme activity, and serves as the core structure for electrochemical coupling. Notably, the hydrophobic spine and the helix proximal to the PD are also conserved in PTEN, suggesting that the voltage-sensitive enzyme activation in VSP relies on structures common to both VSP and PTEN.

Materials and Methods

Molecular Biology. All VSP mutants were constructed from WT Ci-VSP in pSD64TF (8). To generate fluorescence-tagged Ci-VSP constructs, mCherry was fused at the C-terminal via a glycine-serine linker. Amino acid mutations were generated by using PrimeSTAR Mutagenesis Basal Kit (Takara Bio Inc.) and were confirmed by DNA sequencing. Mouse $K_{ir}3.2d$ (GIRK2d) (56) was a kind gift from Yoshihisa Kurachi (Osaka University, Osaka, Japan). Bovine G protein β and γ (Gβ and Gγ) (57) were kindly provided by Toshihide Nukada (retired). The pAnap plasmid (Addgene ID: 48696) (58) encoding transfer RNA (tRNA) and aminoacyl-tRNA synthetase was obtained from Addgene and was identical to that used in our previous studies (17, 21).

Oocyte Preparation. Oocytes were collected from *Xenopus laevis* as previously described (8, 10) in accordance with the guidelines of the Animal Care and Use Committee of the Osaka University Graduate School of Medicine. Defolliculated oocytes were injected with 50 nL of cRNA transcribed in vitro using an mMES-SAGE mMACHINE kit (Thermo Fisher Scientific) and were maintained in ND96 solution (96 mM NaCl, 2 mM KCl, 1.8 mM $CaCl_2$, 1 mM $MgCl_2$, and 5 mM 2-[4-(2-Hydroxyethyl)-1-piperazinyl]ethanesulfonic acid (Hepes), pH 7.5, with NaOH) supplemented with 0.1 mg/mL gentamycin (FUJIFILM Wako Pure Chemical Corporation or Nacalai Tesque, Inc.) and 5 mM sodium pyruvate until recording. The incubation temperature was 18 °C except for toxic constructs, which were incubated at 12 °C and then 18 °C to minimize damage to the plasma membrane.

TEVC of *Xenopus* Oocyte. The TEVC was performed using an Oocyte Clamp amplifier (OC-725C: Warner Instruments) at room temperature (20 to 26 °C). The glass microelectrodes were filled with 2 M potassium acetate and 1 M KCl solution or 3 M KCl solution, and their resistances ranged from 0.1 to 1.0 MΩ. ND96 solution or SC control solution (100 mM N-Methyl-D-glucamine [NMDG], 2 mM KCl, 5 mM $MgCl_2$, and 5 mM Hepes, pH 7.6, with HCl) was used as the bath solution. Holding potential was at −60 mV unless otherwise noted.

To evaluate the phosphatase activity of Ci-VSP, WT or mutant Ci-VSP was coexpressed with $K_{ir}3.2d$, Gβ, and Gγ on the same oocyte. Output signals were digitized at 10 kHz through an analog-to-digital/digital-to-analog (AD/DA) converter (InstruTECH LIH 8 + 8: HEKA Elektronik or Digidata 1440A: Molecular Devices) running under PatchMaster software (HEKA Elektronik) or pClamp software (Molecular Devices), respectively. Sensing current was also measured from the same oocyte to assess Ci-VSP expression level.

To evaluate the charge–voltage relationship, sensing current was measured from oocytes expressing Ci-VSP alone in SC control solution. Sensing currents were evoked by depolarizing steps from the holding potential of −60 mV or −80 mV to 150 mV or 200 mV in 10-mV increments. Leak subtraction was performed using a P/-8 protocol.

A cysteine cross-link experiment was performed using three methods: TEVC, on-cell patch recording, and VCF. In the TEVC recording, sensing currents were measured repeatedly to confirm a disulfide bond formation between a pair of cysteines. Sensing currents were evoked to 150 mV every 15 s, whereas in oocytes expressing H237C/L284C mutant, voltage was stepped also to 100 mV and 130 mV (*SI Appendix,* Fig. S16H). Recordings were stopped after the 15th measurement or when the decrease of sensing current amplitude was saturated. The bath solution was SC control solution, and 100 mM DTT (FUJIFILM Wako

Pure Chemical Corporation) in the bath solution was used for 5-min preincubation at 18 °C for H237C/L284C mutant–expressing oocytes.

Oocyte Patch-Clamp Recording in Cysteine Cross-Link Study. Sensing current recordings in the on-cell patch configuration were done using an Axopatch-200B amplifier (Molecular Devices) through an AD/DA converter (Digidata 1322A: Molecular Devices) running under pClamp software. Current traces were filtered at 5 kHz using a four-pole Bessel filter and sampled at 100 kHz. Leak currents were subtracted by using a P/-8 protocol. Vitelline membrane was removed manually using forceps after incubation for 1 to 5 min in a hypertonic solution containing 192 mM NMDG, 4 mM KCl, 3.6 mM $CaCl_2$, 2 mM $MgCl_2$, and 10 mM Hepes, pH 7.4, with HCl. Patch pipettes were pulled from borosilicate glass (Drummond Scientific Company), and their resistances were 0.8 to 1.9 MΩ after filling with the solution containing 105 mM NMDG, 2 mM $CaCl_2$, and 10 mM Hepes (pH 7.5 with methanesulfonic acid). To match the recording condition with that under TEVC, NMDG-based bath solution (105 mM NMDG, 2 mM $MgCl_2$, 0.1 mM ethylene glycol-bis(2-aminoethylether)-N,N,N',N'-tetraacetic acid (EGTA), and 10 mM Hepes, pH 7.5, with methanesulfonic acid) was used. Sensing currents were evoked by depolarizing steps from the holding potential of −60 mV to 180 mV in 30-mV increments, and the set of step pulses was repeated 20 times and acquired data were averaged. The charge–voltage relationships of sensing currents in the on-cell configuration measured in the NMDG-based bath solution were similar to those in high K^+ bath solution (92 mM KCl, 0.75 mM $CaCl_2$, 1 mM $MgCl_2$, and 10 mM Hepes, pH 7.5, with KOH) (*SI Appendix*, Fig. S17F). This suggests that resting membrane potential of the oocyte was near zero under the NMDG-based bath solution.

For cysteine cross-link experiments, injected oocytes were incubated for 36 h at 12 °C and then 6 to 12 h at 18 °C to minimize damage to the plasma membrane. Patch membranes were repeatedly depolarized from the holding potential of −60 mV to 150 mV every 15 s. Recordings were stopped after the 10th measurement or when the decrease of sensing current amplitude was saturated. Ten sweeps were averaged to obtain current traces and plots of time-dependent changes in Q_{OFF}.

VCF. For VCF (24) with TMRM (Invitrogen), the target labeling site was substituted for a cysteine in Ci-VSP. At 60 to 72 h after injection, oocytes were incubated in ND96 solution with 10 μM TMRM at 18 °C for 1 h in the dark. Labeled oocytes were then rinsed in TMRM-free ND96 solution twice and kept in the dark until recording.

Fluorescence imaging was performed under TEVC using an inverted fluorescence microscope (model IX71: Olympus) equipped with a 20x 0.75 numerical aperture (N.A.) objective (Olympus), an Oocyte Clamp amplifier (OC-725C), and a filter cube composed of an excitation filter (531 nm/40 nm BrightLine: Semrock), an emission filter (593 nm/40 nm BrightLine: Semrock), and a dichroic (DM562: Semrock). The oocytes were illuminated by a 100-W mercury arc ramp (Olympus), and emitted fluorescence was detected by a photomultiplier tube (H10722-20: Hamamatsu Photonics). The output signals from the photomultiplier tube were digitized at 10 kHz with an AD/DA converter (Digidata 1440A) and analyzed using pClamp software. Fluorescence changes were elicited by voltage steps to 200 mV in 10-mV increments. The set of step pulses was repeated eight times, and acquired fluorescence data were averaged.

A cysteine cross-link experiment in combination with VCF with TMRM was performed using oocytes incubated for 48 h at 12 °C and then 11 h at 18 °C after injection. Labeled oocytes were bathed in SC control solution. After measurement of fluorescence in response to single depolarization to 150 mV, sensing currents were measured repeatedly every 15 s as described above. After the 15th measurement or when the decrease of sensing current amplitude was saturated, fluorescence measurement was performed in the same oocyte again. The pulse to evoke the fluorescence change was repeated three times, and acquired data were averaged when the amplitude of fluorescence change was small.

VCF with Anap (FutureChem Co., Ltd.) was conducted as described previously (17, 21). For expression of Ci-VSPs harboring Anap, 20 nL of pAnap plasmid solution (200 ng/μL) was injected into the nucleus of oocytes, and the oocytes were incubated for 24 h in ND96 solution. Then, cRNAs encoding Ci-VSP in which the target site was mutated to an *amber* nonsense codon (TAG) were mixed with 1 mM Anap at a ratio of 1:1, and 50 nL of this mixture was injected

into the cytoplasm of the oocytes under a dim red light to prevent photobleaching. The injected oocytes were maintained for 60 to 72 h in the dark.

The experimental setup for Anap fluorescence measurement was the same as that for TMRM fluorescence measurement, except for the following points. Light was filtered through a BP330-385 excitation filter and a DM400 dichroic (Olympus). The fluorescence from oocytes was split by a dichroic (DM458: Semrock) and emitted separately by two different emission filters (BA420-460 and BA460-510: Olympus). The emitted fluorescence was detected by two photomultiplier tubes. Fluorescence changes were elicited by both depolarizing and hyperpolarizing steps from the holding potential of −60 mV to 180 mV in 20-mV increments and from the holding potential of −20 mV to −180 mV in 20-mV decrements, respectively. The set of step pulses was repeated 16 times, and acquired fluorescence data were averaged.

Measurement of Anap Spectrum. Spectrum of Anap incorporated into Ci-VSP expressed in oocytes was measured under TEVC. The bath solution was ND96 solution. Spectral measurement was performed using an inverted fluorescence microscope (model IX73: Olympus) with a 20x 0.75 N.A. objective (Olympus) at room temperature (22 to 24 °C). Anap fluorescence was excited by a 75-W Xenon arc ramp (Olympus) with a BP330-385 excitation filter and a DM400 dichroic (Olympus) (*SI Appendix*, Fig. S12A). mCherry was excited with an excitation filter (542 nm/20 nm BrightLine: Semrock), an emission filter (620 nm/52 nm BrightLine: Semrock), and a dichroic (FF570-Di01: Semrock). Emission spectrum was collected by a spectrograph (Acton SpectraPro 2150i, 300-g/mm grating, 500-nm blaze: Teledyne Princeton Instruments) in conjunction with an electron-multiplying charge-coupled device camera (C9100-13: Hamamatsu Photonics), which was controlled by MetaMorph software (Molecular Devices). Spectral images were collected with a 200-ms exposure through a slit (width: 95 μm). Data were analyzed using ImageJ software (NIH). Spectra were extracted from acquired spectral images (*SI Appendix*, Fig. S12B) by averaging 25 vertical pixels over a region of interest. Emission peak value of Anap was found by fitting the spectrum with a skewed Gauss distribution using Microsoft Excel 2016 software. Similar fitting was made by using Igor Pro software (WaveMetrics).

A pilot test of quenching of Anap fluorescence by tryptophan (*SI Appendix*, Fig. S10 *A and B*) was performed using a mixture of Anap and tryptophan solution with the same apparatus as in the spectral analysis from oocyte. Anap solution was prepared at 10 μM in 20 mM Tris·HCl (pH 8.0). L-Tryptophan (Sigma-Aldrich) and L-Alanine (FUJIFILM Wako Pure Chemical Corporation) were dissolved in 10 μM Anap solution. The quenching effect of tryptophan on Anap fluorescence was estimated by the Stern-Volmer equation: $F_0/F = 1 + K_{SV}[\text{Trp}]$, where F_0 is the Anap fluorescence at the emission peak in the absence of tryptophan, F is the Anap fluorescence at the emission peak with each concentration of tryptophan, K_{SV} is the Stern-Volmer quenching constant, and [Trp] is the tryptophan concentration.

Structural Modeling with ColabFold. ColabFold (34) is an opensource software for protein structure prediction that combines fast multiple sequence alignment generation with AlphaFold2 (59). Using the basic Notebook of ColabFold on Google Colab, AlphaFold2 _mmseqs2 (60), the full-length Ci-VSP, Dr-VSP, and human PTEN structures were predicted. Input amino acid sequences are as follows: WT Ci-VSP, M1 to I576 (NM_001033826.1); WT Dr-VSP, M1 to P511 (NM_001025458.1); and WT human PTEN, M1 to V403 (NM_000314.8). We selected the structures that had the best predicted local distance difference test. Figures were prepared using PyMOL (Schrödinger, Inc.), and N-terminal intracellular linkers of VSPs and the C-terminal tail of PTEN were missed for clarity.

Data Analysis. Data are presented as mean ± SD except for the ΔF/F versus voltage relationship of Anap, for which data are presented as mean ± SEM. Data analyses were performed using Microsoft Excel 2016, PatchMaster, Clampfit (Molecular Devices), and Igor Pro software. Statistical tests were conducted using Microsoft Excel 2016 and R statistical software.

The phosphatase activity of VSP was taken as the rate constant, which was determined by fitting of a normalized K_{ir} current decay with a single exponential function (21–23) (*SI Appendix*, Fig. S1 *A and B*). Q_{OFF}-V curves and F-V curves of G214C* mutants were fitted with the Boltzmann equation: $Q(V)/Q_{max}$ or $F(V)/F_{max} = 1/\{1 + \exp[−(V − V_{1/2})/\beta]\}$, where β is the slope factor and $V_{1/2}$ is the half-maximum potential at which $Q(V) = Q_{max}/2$ or $F(V) = F_{max}/2$. β is expressed

as $\beta = kT/ze_0$, where k is the Boltzmann's constant, T is the absolute temperature, z is the effective valence, and e_0 is the elementary charge. In some mutants where the Q_{OFF} did not clearly saturate within the experimental voltage range, the fitting of Q_{OFF}-V curves was performed on the stipulation that $0 < Q(V) < 1$.

Data Availability. All study data are included in the article and/or *SI Appendix*.

Author affiliations: [a]Laboratory of Integrative Physiology, Department of Physiology, Graduate School of Medicine, Osaka University, Suita, Osaka 565-0871, Japan; [b]Institute for Protein Research, Osaka University, Suita, Osaka 565-0871, Japan; and [c]Graduate School of Frontier Biosciences, Osaka University, Suita, Osaka 565-0871, Japan

1. F. Bezanilla, The voltage sensor in voltage-dependent ion channels. *Physiol. Rev.* **80**, 555–592 (2000).
2. P. A. Slesinger, Y. N. Jan, L. Y. Jan, The S4-S5 loop contributes to the ion-selective pore of potassium channels. *Neuron* **11**, 739–749 (1993).
3. M. C. Sanguinetti, Q. P. Xu, Mutations of the S4-S5 linker alter activation properties of HERG potassium channels expressed in *Xenopus* oocytes. *J. Physiol.* **514**, 667–675 (1999).
4. S. B. Long, E. B. Campbell, R. MacKinnon, Voltage sensor of Kv1.2: Structural basis of electromechanical coupling. *Science* **309**, 903–908 (2005).
5. T. Kalstrup, R. Blunck, S4-S5 linker movement during activation and inactivation in voltage-gated K+ channels. *Proc. Natl. Acad. Sci. U.S.A.* **115**, E6751–E6759 (2018).
6. G. Wisedchaisri et al., Resting-state structure and gating mechanism of a voltage-gated sodium channel. *Cell* **178**, 993–1003.e12 (2019).
7. P. Hou et al., Two-stage electro-mechanical coupling of a Kv channel in voltage-dependent activation. *Nat. Commun.* **11**, 676 (2020).
8. Y. Murata, H. Iwasaki, M. Sasaki, K. Inaba, Y. Okamura, Phosphoinositide phosphatase activity coupled to an intrinsic voltage sensor. *Nature* **435**, 1239–1243 (2005).
9. Y. Okamura, A. Kawanabe, T. Kawai, Voltage-sensing phosphatases: Biophysics, physiology, and molecular engineering. *Physiol. Rev.* **98**, 2097–2131 (2018).
10. Y. Murata, Y. Okamura, Depolarization activates the phosphoinositide phosphatase Ci-VSP, as detected in *Xenopus* oocytes coexpressing sensors of PIP2. *J. Physiol.* **583**, 875–889 (2007).
11. H. Iwasaki et al., A voltage-sensing phosphatase, Ci-VSP, which shares sequence identity with PTEN, dephosphorylates phosphatidylinositol 4,5-bisphosphate. *Proc. Natl. Acad. Sci. U.S.A.* **105**, 7970–7975 (2008).
12. T. Kawai et al., Polarized PtdIns(4,5)P2 distribution mediated by a voltage-sensing phosphatase (VSP) regulates sperm motility. *Proc. Natl. Acad. Sci. U.S.A.* **116**, 26020–26028 (2019).
13. S. Sakata, M. I. Hossain, Y. Okamura, Coupling of the phosphatase activity of Ci-VSP to its voltage sensor activity over the entire range of voltage sensitivity. *J. Physiol.* **589**, 2687–2705 (2011).
14. S. S. Grimm, E. Y. Isacoff, Allosteric substrate switching in a voltage-sensing lipid phosphatase. *Nat. Chem. Biol.* **12**, 261–267 (2016).
15. S. C. Kohout et al., Electrochemical coupling in the voltage-dependent phosphatase Ci-VSP. *Nat. Chem. Biol.* **6**, 369–375 (2010).
16. P. M. Castle, K. D. Zolman, S. C. Kohout, Voltage-sensing phosphatase modulation by a C2 domain. *Front. Pharmacol.* **6**, 1–15 (2015).
17. S. Sakata, Y. Jinno, A. Kawanabe, Y. Okamura, Voltage-dependent motion of the catalytic region of voltage-sensing phosphatase monitored by a fluorescent amino acid. *Proc. Natl. Acad. Sci. U.S.A.* **113**, 7521–7526 (2016).
18. C. A. Villalba-Galea, F. Miceli, M. Taglialatela, F. Bezanilla, Coupling between the voltage-sensing and phosphatase domains of Ci-VSP. *J. Gen. Physiol.* **134**, 5–14 (2009).
19. K. Hobiger, T. Utesch, M. A. Mroginski, T. Friedrich, Coupling of Ci-VSP modules requires a combination of structure and electrostatics within the linker. *Biophys. J.* **102**, 1313–1322 (2012).
20. L. Liu et al., A glutamate switch controls voltage-sensitive phosphatase function. *Nat. Struct. Mol. Biol.* **19**, 633–641 (2012).
21. A. Kawanabe et al., The hydrophobic nature of a novel membrane interface regulates the enzyme activity of a voltage-sensing phosphatase. *eLife* **7**, e41653 (2018).
22. A. Kawanabe et al., Engineering an enhanced voltage-sensing phosphatase. *J. Gen. Physiol.* **152**, e201912491 (2020).
23. H. Tsutsui, N. Mizutani, Y. Okamura, "Engineering voltage sensing phosphatase (VSP)" in *Methods in Enzymology*, D. L. Minor Jr., H. M. Colecraft, Eds. (Elsevier, 2021), pp. 85–114.
24. L. M. Mannuzzu, M. M. Moronne, E. Y. Isacoff, Direct physical measure of conformational rearrangement underlying potassium channel gating. *Science* **271**, 213–216 (1996).
25. S. C. Kohout, M. H. Ulbrich, S. C. Bell, E. Y. Isacoff, Subunit organization and functional transitions in Ci-VSP. *Nat. Struct. Mol. Biol.* **15**, 106–108 (2008).
26. J. Kyte, R. F. Doolittle, A simple method for displaying the hydropathic character of a protein. *J. Mol. Biol.* **157**, 105–132 (1982).
27. B. Nölting, "Physical interactions that determine the properties of proteins" in *Protein Folding Kinetics*, B. Nölting, Ed. (Springer Berlin Heidelberg, 1999), pp. 17–25.
28. H. S. Lee, J. Guo, E. A. Lemke, R. D. Dimla, P. G. Schultz, Genetic incorporation of a small, environmentally sensitive fluorescent probe into proteins in *Saccharomyces cerevisiae*. *J. Am. Chem. Soc.* **131**, 12921–12923 (2009).
29. S. E. Mansoor, H. S. McHaourab, D. L. Farrens, Mapping proximity within proteins using fluorescence spectroscopy. A study of T4 lysozyme showing that tryptophan residues quench bimane fluorescence. *Biochemistry* **41**, 2475–2484 (2002).
30. S. E. Mansoor, M. A. Dewitt, D. L. Farrens, Distance mapping in proteins using fluorescence spectroscopy: The tryptophan-induced quenching (TrIQ) method. *Biochemistry* **49**, 9722–9731 (2010).
31. E. E. L. Lee, F. Bezanilla, Methodological improvements for fluorescence recordings in *Xenopus laevis* oocytes. *J. Gen. Physiol.* **151**, 264–272 (2019).
32. Q. Li et al., Structural mechanism of voltage-dependent gating in an isolated voltage-sensing domain. *Nat. Struct. Mol. Biol.* **21**, 244–252 (2014).
33. C. L. Careaga, J. J. Falke, Thermal motions of surface α-helices in the D-galactose chemosensory receptor. Detection by disulfide trapping. *J. Mol. Biol.* **226**, 1219–1235 (1992).
34. M. Mirdita et al., ColabFold: Making protein folding accessible to all. *Nat. Methods* **19**, 679–682 (2022).
35. R. Shen, Y. Meng, B. Roux, E. Perozo, Mechanism of voltage gating in the voltage-sensing phosphatase Ci-VSP. *bioRxiv* [Preprint] (2022). https://doi.org/10.1101/2022.02.17.480971 (Accessed 18 February 2022).
36. J.-O. Lee et al., Crystal structure of the PTEN tumor suppressor: Implications for its phosphoinositide phosphatase activity and membrane association. *Cell* **99**, 323–334 (1999).
37. D. R. Dempsey et al., The structural basis of PTEN regulation by multi-site phosphorylation. *Nat. Struct. Mol. Biol.* **28**, 858–868 (2021).
38. H. C. Tsou et al., The role of MMAC1 mutations in early-onset breast cancer: Causative in association with Cowden syndrome and excluded in BRCA1-negative cases. *Am. J. Hum. Genet.* **61**, 1036–1043 (1997).
39. S. A. Byron et al., Inhibition of activated fibroblast growth factor receptor 2 in endometrial cancer cells induces cell death despite PTEN abrogation. *Cancer Res.* **68**, 6902–6907 (2008).
40. S. Dan et al., Correlating phosphatidylinositol 3-kinase inhibitor efficacy with signaling pathway status: In silico and biological evaluations. *Cancer Res.* **70**, 4982–4994 (2010).
41. Q. Wang, Y. Wei, M. Mottamal, M. F. Roberts, G. Krilov, Understanding the stereospecific interactions of 3-deoxyphosphatidylinositol derivatives with the PTEN phosphatase domain. *J. Mol. Graph. Model.* **29**, 102–114 (2010).
42. F. Hsu et al., Structural basis for substrate recognition by a unique *Legionella* phosphoinositide phosphatase. *Proc. Natl. Acad. Sci. U.S.A.* **109**, 13567–13572 (2012).
43. L. Trésaugues et al., Structural basis for phosphoinositide substrate recognition, catalysis, and membrane interactions in human inositol polyphosphate 5-phosphatases. *Structure* **22**, 744–755 (2014).
44. J. Paesmans et al., A structure of substrate-bound Synaptojanin1 provides new insights in its mechanism and the effect of disease mutations. *eLife* **9**, e64922 (2020).
45. M. J. Begley et al., Molecular basis for substrate recognition by MTMR2, a myotubularin family phosphoinositide phosphatase. *Proc. Natl. Acad. Sci. U.S.A.* **103**, 927–932 (2006).
46. R. B. Campbell, F. Liu, A. H. Ross, Allosteric activation of PTEN phosphatase by phosphatidylinositol 4,5-bisphosphate. *J. Biol. Chem.* **278**, 33617–33620 (2003).
47. G. Denning, B. Jean-Joseph, C. Prince, D. L. Durden, P. K. Vogt, A short N-terminal sequence of PTEN controls cytoplasmic localization and is required for suppression of cell growth. *Oncogene* **26**, 3930–3940 (2007).
48. H.-N. Nguyen et al., Engineering ePTEN, an enhanced PTEN with increased tumor suppressor activities. *Proc. Natl. Acad. Sci. U.S.A.* **111**, E2684–E2693 (2014).
49. S. B. Johnston, R. T. Raines, Catalysis by the tumor-suppressor enzymes PTEN and PTEN-L. *PLoS One* **10**, e0116898 (2015).
50. J. Lacroix et al., Controlling the activity of a phosphatase and tensin homolog (PTEN) by membrane potential. *J. Biol. Chem.* **286**, 17945–17953 (2011).
51. A. Mavrantoni et al., A method to control phosphoinositides and to analyze PTEN function in living cells using voltage sensitive phosphatases. *Front. Pharmacol.* **6**, 1–13 (2015).
52. F. Vazquez, S. Ramaswamy, N. Nakamura, W. R. Sellers, Phosphorylation of the PTEN tail regulates protein stability and function. *Mol. Cell. Biol.* **20**, 5010–5018 (2000).
53. M. Rahdar et al., A phosphorylation-dependent intramolecular interaction regulates the membrane association and activity of the tumor suppressor PTEN. *Proc. Natl. Acad. Sci. U.S.A.* **106**, 480–485 (2009).
54. M. Matsuda et al., Crystal structure of the cytoplasmic phosphatase and tensin homolog (PTEN)-like region of *Ciona intestinalis* voltage-sensing phosphatase provides insight into substrate specificity and redox regulation of the phosphoinositide phosphatase activity. *J. Biol. Chem.* **286**, 23368–23377 (2011).
55. T. Kurokawa et al., 3′ Phosphatase activity toward phosphatidylinositol 3,4-bisphosphate [PI(3,4)P2] by voltage-sensing phosphatase (VSP). *Proc. Natl. Acad. Sci. U.S.A.* **109**, 10089–10094 (2012).
56. A. Inanobe et al., Molecular cloning and characterization of a novel splicing variant of the Kir3.2 subunit predominantly expressed in mouse testis. *J. Physiol.* **521**, 19–30 (1999).
57. T. Furukawa et al., Differential interactions of the C terminus and the cytoplasmic I-II loop of neuronal Ca2+ channels with G-protein α and β γ subunits. II. Evidence for direct binding. *J. Biol. Chem.* **273**, 17595–17603 (1998).
58. A. Chatterjee, J. Guo, H. S. Lee, P. G. Schultz, A genetically encoded fluorescent probe in mammalian cells. *J. Am. Chem. Soc.* **135**, 12540–12543 (2013).
59. J. Jumper et al., Highly accurate protein structure prediction with AlphaFold. *Nature* **596**, 583–589 (2021).
60. M. Mirdita, S. Ovchinnikov, M. Steinegger, ColabFold - Making protein folding accessible to all (v1.0-alpha). *Zenodo*. 10.5281/ZENODO.5123297. Deposited 22 July 2021.